# RESEARCH ARTICLE

**Key Points:**
- Current-sheet thicknesses affect the high-frequency breakpoint frequency of the solar wind
- Solar-wind current sheets contain substantial magnetic Fourier power
- There are outstanding questions about the solar-wind current sheet origins and physics

**Correspondence to:**
J. E. Borovsky,
jborovsky@spacescience.org

# Exploring the effect of current sheet thickness on the high-frequency Fourier spectrum breakpoint of the solar wind

Joseph E. Borovsky[1,2] and John J. Podesta[1]

[1]Center for Space Plasma Physics, Space Science Institute, Boulder, Colorado, USA, [2]Climate and Space Sciences and Engineering, University of Michigan, Ann Arbor, Michigan, USA

**Abstract** The magnetic power spectrum of the solar wind at 1 AU exhibits a breakpoint at a frequency of about $0.1–1\,Hz$, with the spectrum being steeper above the breakpoint than below the breakpoint. Because magnetic discontinuities contain much of the Fourier power in the solar wind, it is suspected that current sheet thicknesses (i.e., discontinuity thicknesses) may play a role in determining the frequency of this breakpoint. Using time series measurements of the solar wind magnetic field from the Wind spacecraft, the effect of current sheet thicknesses on the breakpoint is investigated by time stretching the solar wind time series at the locations of current sheets, effectively thickening the current sheets in the time series. This localized time stretching significantly affects the magnetic power spectral density of the solar wind in the vicinity of the high-frequency breakpoint: a substantial fraction of the Fourier power at the breakpoint frequency is contained in current sheets that occupy a small fraction of the spatial volume of the solar wind. It is concluded that current sheet thickness appears to play a role in determining the frequency $f_B$ of the high-frequency breakpoint of the magnetic power spectrum of the solar wind. This analysis of solar wind data is aided by comparisons with power spectra generated from artificial time series.

## 1. Introduction

The solar wind plasma is endowed with large numbers of current sheets [*Siscoe et al.*, 1968; *Vasquez et al.*, 2007; *Borovsky*, 2008]. As the solar wind magnetic field structure advects past a spacecraft the current sheets are seen in the time series of magnetic field measurements as sudden large changes in the direction of the solar wind magnetic field (i.e., as directional discontinuities) [*Burlaga*, 1969; *Bruno et al.*, 2001; *Li*, 2008]. In the slow (streamer belt) solar wind, the current sheets also take the form of sudden changes in the strength of the solar wind magnetic field (pressure balance structures) [*Burlaga and Ness*, 1969; *Franz et al.*, 2000; *Dalin et al.*, 2002; *Barkhatov et al.*, 2003]. Often, the current sheets form boundaries between plasmas of different types [*Riazantseva et al.*, 2005a, 2005b; *Borovsky*, 2012a]. Some current sheets are Alfvenic, with strong velocity shear accompanying the magnetic field rotation [*Neugebauer et al.*, 1984, 1986; *Neugebauer*, 1985; *Borovsky*, 2012b]; some are not Alfvenic. The origins of the current sheets in the solar wind plasma are not known [e.g., *Neugebauer and Alexander*, 1991; *Neugebauer*, 2006; *Malaspina and Gosling*, 2012; *Roberts*, 2012]. It has been argued that large-angle magnetic field rotations are of solar origin and smaller-angle rotations are turbulence [*Neugebauer and Giacalone*, 2010; *Owens et al.*, 2011], but there are contrary views [*Vasquez and Hollweg*, 1999; *Tsurutani and Ho*, 1999; *Greco et al.*, 2009; *Zhdankin et al.*, 2012].

The magnetic field power spectral density of the solar wind is famously characterized by a power law shape in an "inertial range" that includes oscillation periods ranging from an hour or more down to the range of a second or so [*Belcher and Davis*, 1971; *Tu and Marsch*, 1995; *Goldstein and Roberts*, 1999; *Podesta et al.*, 2007; *Bruno and Carbone*, 2013]. At a frequency on the order of $1\,Hz$, the magnetic spectrum of the solar wind has a breakpoint with a significantly steeper spectrum above the breakpoint than below [e.g., *Behannon*, 1978; *Goldstein et al.*, 1995; *Leamon et al.*, 1998; *Markovskii et al.*, 2008; *Bourouaine et al.*, 2012; *Chen et al.*, 2014; *Bruno and Trenchi*, 2014]. Much work has been performed looking into the physical cause of this high-frequency (short-wavelength) spectral breakpoint: most of the work focusing on the kinetic damping of plasma wave modes [e.g., *Gary*, 1999; *Leamon et al.*, 1998, 1999; *Gary and Borovsky*, 2004; *Howes et al.*, 2008; *Podesta*, 2012] and on the dispersion of plasma wave modes [e.g., *Stawicki et al.*, 2001; *Saito et al.*, 2010; *Sahraoui et al.*, 2010, 2012; *TenBarge et al.*, 2012], and some focusing on magnetic structures and reconnection [e.g., *Leamon et al.*, 2000.
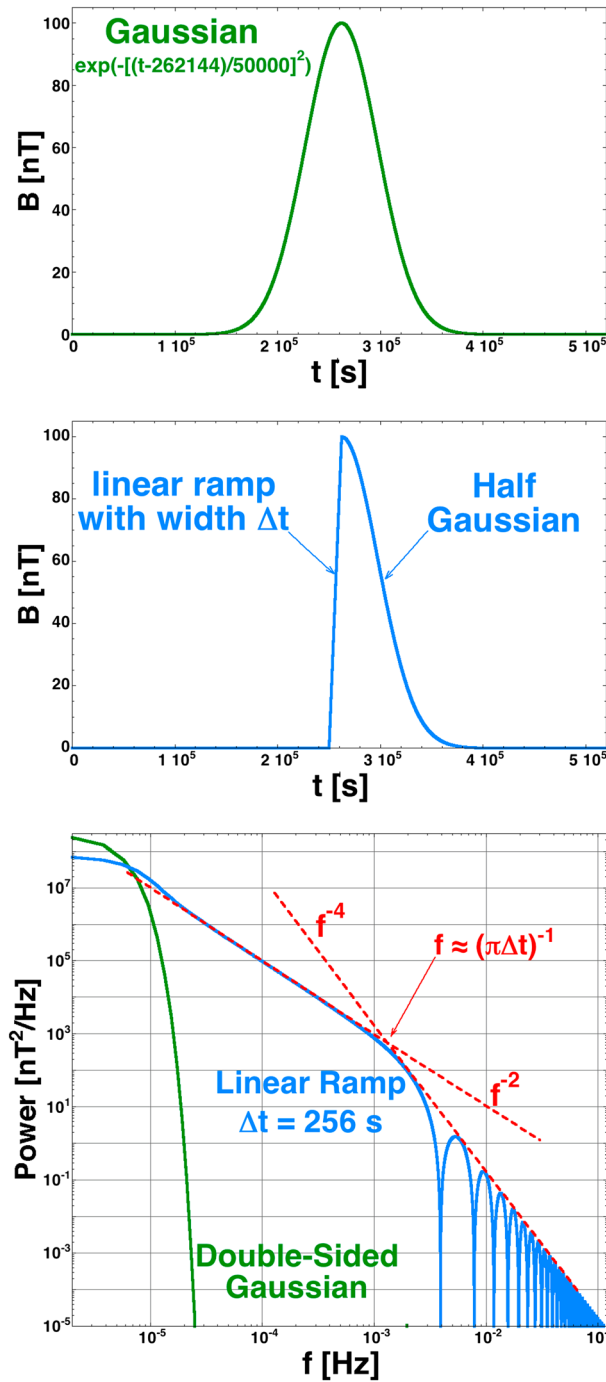
**Figure 1.** (top) An artificial time series composed of a single Gaussian pulse. (middle) An artificial time series composed of half of a Gaussian pulse matched onto a linear ramp. (bottom) The power spectral densities of the two time series of the top and middle panel are plotted.

The current sheets (discontinuities) of the solar wind carry much of the Fourier power and strongly affect the power spectral density of the magnetic field [*Siscoe et al.*, 1968; *Sari and Ness*, 1969; *Borovsky*, 2010; *Li et al.*, 2011]. Magnetic discontinuities strongly affect the inertial range portion of the magnetic power spectral density of the solar wind, with the occurrence rate statistics and size distribution affecting the spectral slope as well as the amplitude of the spectrum. Relatedly, for some time it has been realized that discontinuities are strong contributors to the intermittency of the solar wind magnetic field time series [cf. *Veltri*, 1999; *Bruno et al.*, 2001; *Mangeney et al.*, 2001].

As will be shown in Figure 1, the Fourier transform of a single linear ramp of thickness $\Delta t$ has a breakpoint (steepening of the spectrum) that occurs at a frequency $f \sim 1/\Delta t$. Because of the significant Fourier power contained in solar wind discontinuities, one might suspect that the high-frequency spectral break in the power spectrum of magnetic field fluctuations is related to the thicknesses of the magnetic discontinuities in the solar wind. This is sensible because the Fourier power should be significantly smaller at time scales much less than the thickness of a current sheet. Indeed, *Chen et al.* [2014] suggested current sheet thickness as a possible cause of the high-frequency breakpoint in the solar wind.

The purpose of this report is to explore the effect of current sheet thickness on the high-frequency breakpoint in the magnetic spectrum of the solar wind at 1 AU. Because the Fourier spectrum of the current sheets cannot be isolated from the Fourier spectrum produced by other fluctuations in the time series, it is difficult to directly discern the influence of discontinuity thicknesses in the solar wind on the solar wind magnetic spectrum. An unusual technique is used here: in the time series of measurements of the solar wind magnetic field, time is stretched (via linear interpolation) only at locations of strong magnetic discontinuities and the effect of this localized stretching on the magnetic power spectra is examined, with special attention paid to the region of the high-frequency breakpoint.

This manuscript is outlined as follows. In section 2 the method used to produce power spectral densities is discussed. In section 3, artificial time series are constructed and Fourier analyzed to discern the expected

features that current sheets produce in magnetic power spectral densities. In section 4, magnetic field measurements from the Wind spacecraft are Fourier analyzed and the measurement time series are modified in a way to discern the impacts of solar wind current sheets on the magnetic power spectra of the solar wind. Conclusions are stated in section 5. The Appendix A contains a discussion about frequencies in the solar wind associated with the advection of ion gyroradius scale size structure and ion inertial length scale size structure past a spacecraft.

## 2. Methods of Spectral Analysis

Power spectral densities $P(f)$ as functions of the frequency $f$ are constructed by the periodogram method [*Otnes and Enochson*, 1972] where $P(f)$ is the square to the fast Fourier transform FFT($f$) with the normalization $P(f) = (\delta t/N) |FFT(f)|^2$, where $N$ is the number of data points in the time series and $\delta t$ is the time resolution in the time series. For the solar wind magnetic field data, the power spectral density is computed separately for each of the three orthogonal components of the magnetic field vector and then all three spectra are summed to obtain the trace spectrum. Following the statistical study of Appendix B of *Borovsky* [2012c], linear detrend of the time series is performed before Fourier transforming and no window is used. A running average of the periodogram power spectral density is performed when $P(f)$ is plotted.

For the purposes of examining the high-frequency breakpoint of the Fourier power spectra, this periodogram method compares favorably with the multitaper spectral estimator technique developed by *Thomson* [1982] and described in detail in the textbook by *Percival and Walden* [1993], as will be seen in section 4. The spectral estimator methodology used to compute the spectra closely follows *Percival and Walden* [1993] except that no zero padding is used at any stage of the calculation. For the multitaper technique, the chosen spectral bandwidth is $2W = 2 \times 10^{-3}$ Hz, the time-bandwidth product or Shannon number is $2WN\Delta t \approx 158$, and each power spectrum is computed as the average of the first 145 eigenspectra.

## 3. Spectra From Artificial Time Series

Figure 1 is constructed to look at the power spectral density of a single current sheet. Two time series of a single component of the magnetic field $\mathbf{B}(t)$ are constructed on a domain that is 524288 s long, which is $2^{19}$ s. The time resolution $\delta t$ in these artificial time series is $\delta t = 1$ s; hence, each series has $N = 524288$ data points. In the first time series there is a single broad Gaussian pulse constructed using the formula $100 \exp\{-[(t - 262144)/50000]^2\}$, where $t$ is in seconds; this Gaussian pulse is shown as the green curve in Figure 1 (top). The power spectral density of that Gaussian temporal pulse is plotted as the green curve in Figure 1 (bottom). Note in Figure 1 (bottom).that this Gaussian pulse contains Fourier power at low frequencies (below 1/50000 s) but no power at middle and high frequencies. The second time series is constructed by replacing the left half of the Gaussian pulse with a linear ramp of width $\Delta t$ that goes from 0 to 100; this time series is shown as the blue curve in Figure 1 (middle). This single linear ramp in $B(t)$ with thickness $\Delta t$ is taken to represent a single current sheet with thickness $\Delta t$. The power spectral density of this linear ramp half Gaussian is plotted as the blue curve in Figure 1 (bottom) for a ramp width $\Delta t = 256$ s. Note the substantial increase in the Fourier power at high frequencies caused by the ramp. The low-frequency Fourier power of the ramp drops by about a factor of 2 in Figure 1 (bottom) since half of the Gaussian is missing in the blue curve in Figure 1 (middle). The power spectrum of the single linear ramp has a power law form $f^{-2}$ for frequencies below $1/\Delta t$ and has a power law form $f^{-4}$ for frequencies above $1/\Delta t$. (Note that if the shape of the ramp was other than linear, this high-frequency portion of the spectrum would differ from $f^{-4}$: the steepness of that spectrum is governed by the number of continuous derivatives in the time series, with the linear ramp having discontinuous first derivatives.). In Figure 1 (bottom) power law fits of $f^{-2}$ and $f^{-4}$ are drawn as the red dashed lines: the intersection of the two red lines can be taken as a measure of the breakpoint frequency $f_B$ of the spectrum. These plots have been repeated for a broad range of $\Delta t$ values, and the resulting breakpoint frequencies $f_B$ for linear ramps can be approximated as

$$f_B \approx (\pi \Delta t)^{-1}, \tag{1}$$

where $\Delta t$ is the thickness of the linear ramp. Note in Figure 1 (bottom) that the first zero (notch) in the power spectral density of this linear ramp occurs at the frequency $f = 1/\Delta t = 1/(256$ s) [cf. *International Telephone and Telegraph Corporation*, 1979, Table 2.B of section 44-5].
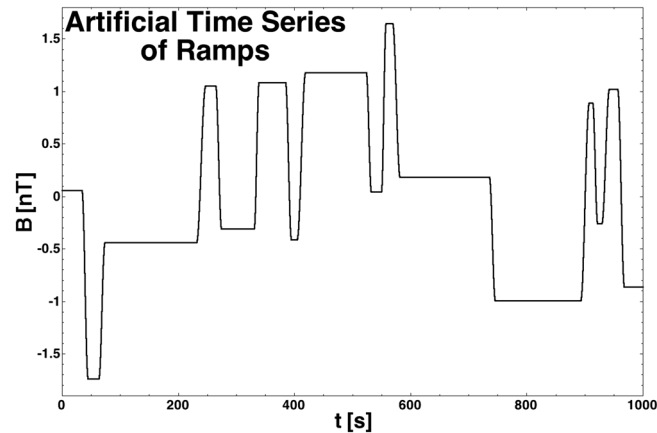
**Figure 2.** The first 1000 s of an artificial time series composed of half sine wave ramps (representing current sheets) occurring with random stretched exponential waiting times.

The effects of multiple current sheets on the power spectra is explored in Figures 2 and 3. In Figure 2 a portion of an artificial time series $B(t)$ is shown, where "current sheets" are represented by half sine wave ramps $\pm A \sin(\pi(t - t_o)/2\Delta t)$ valid for $-\Delta t \le t - t_o \le \Delta t$. These current sheets appear as the vertical jumps in the time series plotted in Figure 2. The amplitudes $A$ of the sine wave ramps are chosen from random numbers between 0.5 and 1.0, and the sign of the ramp is taken to be negative if the value of the function at the start of the ramp is positive, and the sign of the ramp is taken to be positive if the value of the function at the start of the ramp is negative. In the time series shown in Figure 2 the widths $\Delta t$ of the current sheets are taken as random values uniformly distributed between $\Delta t = \Delta t_{\min} = 4$ s and $\Delta t = \Delta t_{\max} = 8$ s. Between the current sheets $B(t)$ is taken to have a constant value. In constructing the artificial time series the waiting times $t_{\text{wait}}$ between current sheet occurrences are taken from a random stretched exponential distribution $\exp(-[t_{\text{wait}}/6.2]^{0.5})$, where $t_{\text{wait}}$ is in units of s. In generating the time series, waiting times that are less than $\Delta t_{\max}$ are discarded and regenerated from the random distribution. In the time series of Figure 2 the waiting times are the flat horizontal regions between the vertical jumps. The full time series of Figure 2 is 47663 s long with a time resolution of 0.092 s and with about 1500 current sheets in the full series. The occurrence rates of the current sheets in the artificial time series is similar to the solar wind observations.

A stretched exponential distribution [*Laherrere and Sornette*, 1998; *Cardona et al.*, 2007] is chosen for the waiting times for two reasons. First, the distribution of waiting times between strong magnetic discontinuities in the solar wind can be well fit by a stretched exponential distribution. For instance, the data used to create the 7 year distribution in Figure 9 of *Borovsky* [2008] can be fit by $44100 \exp[-(t_{\text{wait}}/c_1)^{0.515}]$ $+ 116 \exp(-t_{\text{wait}}/c_2)$, where $c_1 = 4.6$ min and $c_2 = 220$ min. The exponential part of this fit, which dominates at large waiting times, may represent the occurrence of ejecta in the solar wind, where ejecta characteristically have an absence of discontinuities. Second, str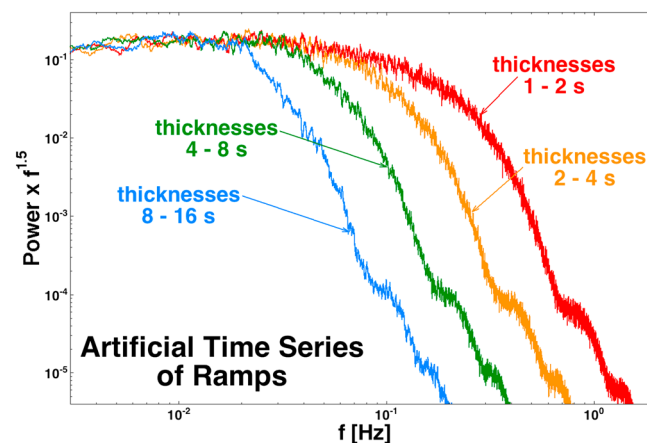etched exponential waiting time distributions lead to power laws in the power spectral densities. This is because stretched exponential distributions of waiting times lead to stretched exponential functional forms of autocorrelation functions [e.g., *Simdyankin and Mousseau*, 2003; *Flomenbom et al.*, 2005; *Pennetta*, 2006]: the Fourier transform of the autocorrelation function is the power spectral density (e.g., equation 6.4.20 of *Tennekes and Lumley* [1972]) and the Fourier transform of a stretched exponential behaves asymptotically like a power law [*Dishon et al.*, 1985; *Montroll and Bender*, 1984; *Wuttke*, 2012].



**Figure 3.** Compensated power spectral densities of artificial time series composed of half sine wave ramps with random stretched exponential waiting times. The power spectra are formed from periodograms with 50-point running averages in $f$.

In Figure 3 the power spectral densities of four artificial time series are shown. The waiting times $t_{\text{wait}}$ in the four time series are taken from the stretched
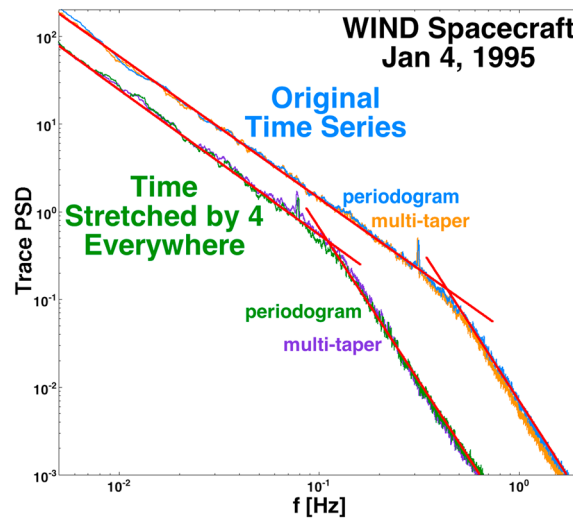
**Figure 4.** The power spectral density of the 4 January 1995 Wind spacecraft magnetic field time series (blue and orange) and the power spectral density of the 4 January magnetic field time series stretched in time everywhere by a factor of 4 (green and purple). The blue and green curves are periodograms, and the orange and purple curves are multitaper spectral estimator plots. The blue periodogram has been smoothed with a 200-point running average, and the green periodogram has been smoothed with a 100-point running average.

exponential distribution $\exp(-[t_{wait}/6.2]^{0.5})$. The ranges of current sheet thicknesses $\Delta t_{min}$ to $\Delta t_{max}$ differ in the four curves. The red curve has current sheet $\Delta t$ values in the range of 1–2 s, the orange curve has $\Delta t$ values in the range of 2–4 s, the green curve has $\Delta t$ in the range of 4–8 s, and the blue curve has $\Delta t$ values in the range of 8–16 s. The green curve is the power spectral density of the time series pre-viewed in Figure 2. The power spectral densities in Figure 3 are compensated spectra, where the power spectral density is multiplied by $f^{1.5}$ before plotting. The four spectra show clear breakpoints from the flatter low-frequency portions to steeper high-frequency portions. The breakpoint frequency $f_B$ of each curve in Figure 3 is determined as the frequency, where a power law fit to the high-frequency curve intersects a power law fit to the low-frequency curve: taking $<\Delta t> = (\Delta t_{max} + \Delta t_{min})/2$ for each of the four curves, this determination yields $f_B \approx (3.3\Delta t)^{-1}$. This is in the ballpark of the rela-tion $f_B \approx (\pi \Delta t)^{-1}$ (expression (1)) found for single linear ramp current sheets.

## 4. Spectra From Solar Wind Time Series and Modified Time Series

To examine the effects that current sheets in the solar wind plasma have on the magnetic power spectral density of the solar wind, 0.092 s time resolution magnetic field measurements from the Magnetic Fields Investigation (MFI) [*Lepping et al.*, 1995] on the Wind spacecraft upstream of the Earth are used from 4 January 1995.

The second day of a 6 day long high-speed stream was on 4 January 1995. The plasma on 4 January was judged to be of coronal hole origin using the *Xu and Borovsky* [2015] categorization scheme, and the high-speed stream was repeating on a 27 day interval. Examining the hourly averaged solar wind values in the OMNI2 database [*King and Papitashvili*, 2005], the number density that day ranged from 2.9 to 4.3 cm$^{-3}$, the proton temperature ranged from 32.0 to 50.4 eV, and the magnetic field strength ranged from 4.5 to 6.5 nT. The solar wind speed $v_{sw}$ ranged from 622 to 706 km/s with a daily average of 664 km/s, the thermal ion gyroradius $r_{gi}$ of the solar wind plasma ranged from 93 to 154 km with an average of 111 km, and the ion inertial length $c/\omega_{pi}$ of the solar wind plasma ranged from 110 to 134 km with an average of 123 km. Advection time scales associated with the $r_{gi}$ and $c/\omega_{pi}$ spatial scales are discussed in Appendix A. The magnetic field on 4 January showed a Parker spiral orientation (with fluctuations), and the magnetic sector during these observations was directed toward the Sun.

The trace-B power spectral density of the first 13.4 hours (524288 data points at 0.092 s time resolution) of magnetic field measurements from WIND on 4 January 1995 is plotted as the blue curve in Figure 4. This blue curve is formed from the periodogram method with a 200-point running average. For comparison the trace-B power spectral density from the multitaper method is plotted in orange. Red lines have been added to guide the eye in the transition from a lower frequency power law to a higher-frequency power law. Note the breakpoint in the spectrum at $f_B \approx 0.4$ Hz and note the spin tone peak at $f \approx 0.31$ Hz.

Plotted as the green curve in Figure 4 is the trace-B power spectral density of the 4 January 1995 WIND magnetic field data stretched everywhere in time by a factor of 4. (And for comparison the purple curve is the trace-B power spectral density formed with the multitaper method.). The time stretching is performed by producing four data points from one data point via linear interpolation. For the pair of adjacent data values ($v_1,v_2$) in the original time series $v_1$ at time $t_o$ and $v_2$ at time $t_o + \delta t$ (where $\delta t$ is
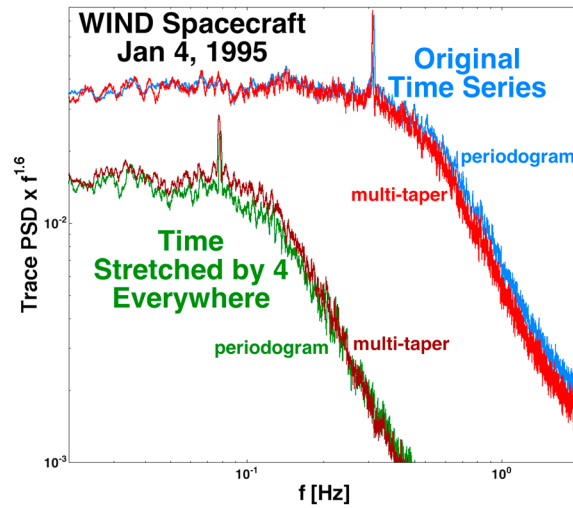
**Figure 5.** Compensated spectral plots of the spectra in Figure 4. For comparison the multitaper spectral estimator (red and dark red) and periodogram (blue and green) methods are both used. The green periodogram is smoothed with a 100-point running average, and the red periodogram is smoothed with a 200-point running average.

the time resolution of the data) in the original series, the corresponding five data points $(w_1, w_2, w_3, w_4, w_5)$ in the new series are

$$w_1(t) = v_1 \tag{2a}$$
$$w_2(t_o + dt) = 0.75\,v_1 + 0.25\,v_2 \tag{2b}$$
$$w_3(t_o + 2dt) = 0.5\,v_1 + 0.5\,v_2 \tag{2c}$$
$$w_4(t_o + 3dt) = 0.25\,v_1 + 0.75\,v_2 \tag{2d}$$
$$w_5(t_o + 4dt) = v_2 \tag{2e}$$

Whereas in the original time series, the transition from value $v_1$ to value $v_2$ occurred in a time $\delta t$, in the new series the transition from value $v_1$ to value $v_2$ occurs in a time $4\delta t$. To produce the green curve in Figure 4, the stretching algorithm of expressions 2a, 2b, 2c, 2d, 2e is applied everywhere in the 4 January time series. Since the original time series has 524288 data points, the fully stretched data set has $4 \times 524288 = 2097152$ data points, but note that only the first 524288 points of the stretched series are used to form the power spectral density of Figure 4.

Comparing the two power spectral densities in Figure 4, it is seen that the spectral breakpoint shifts by a factor of 4 in frequency from $f_B \approx 0.4$ Hz to $f_B \approx 0.1$ Hz and the Wind spacecraft spin tone shifts from $f \approx 0.31$ Hz to $f \approx 0.078$ Hz.
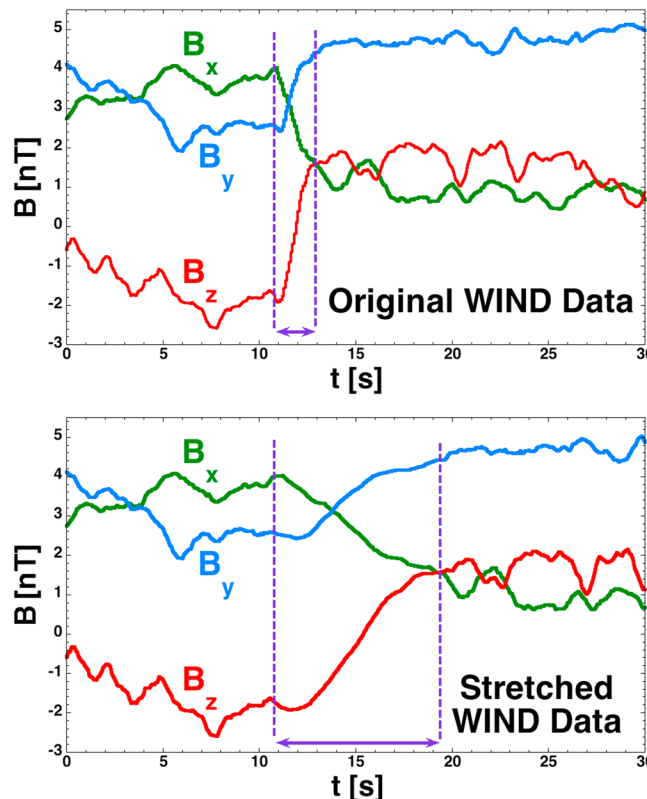


To more clearly see the spectral breakpoint, the blue and green curves of Figure 4 are plotted as compensated spectra in Figure 5 by multiplying the power spectral densities by $f^{1.6}$ before plotting. Note the decreased amplitude of the time stretched green curve compared with the blue curve in Figure 5: this decrease is owed to the Fourier components of the green curve being shifted to lower frequencies, where they are multiplied by smaller $f^{1.6}$ values than the Fourier components of the original blue curve.



**Figure 6.** An example of the time stretching (by a factor of 4) of a current sheet in the 4 January 1995 solar wind data.

To isolate the effects of current sheets on the Fourier spectra, the solar wind magnetic field measurement time series is modified by identifying the location of current sheets in the time series and then using the algorithm of expressions 2a, 2b, 2c, 2d, 2e to stretch the time only in the current sheets by a factor of 4. This acts to thicken the current sheets by a factor of 4 while leaving the rest of the time series unchanged. An example of this current sheet stretching appears in Figure 6. In Figure 6 (top) a 30 s interval of the magnetic field time series from the Wind spacecraft is plotted, with the
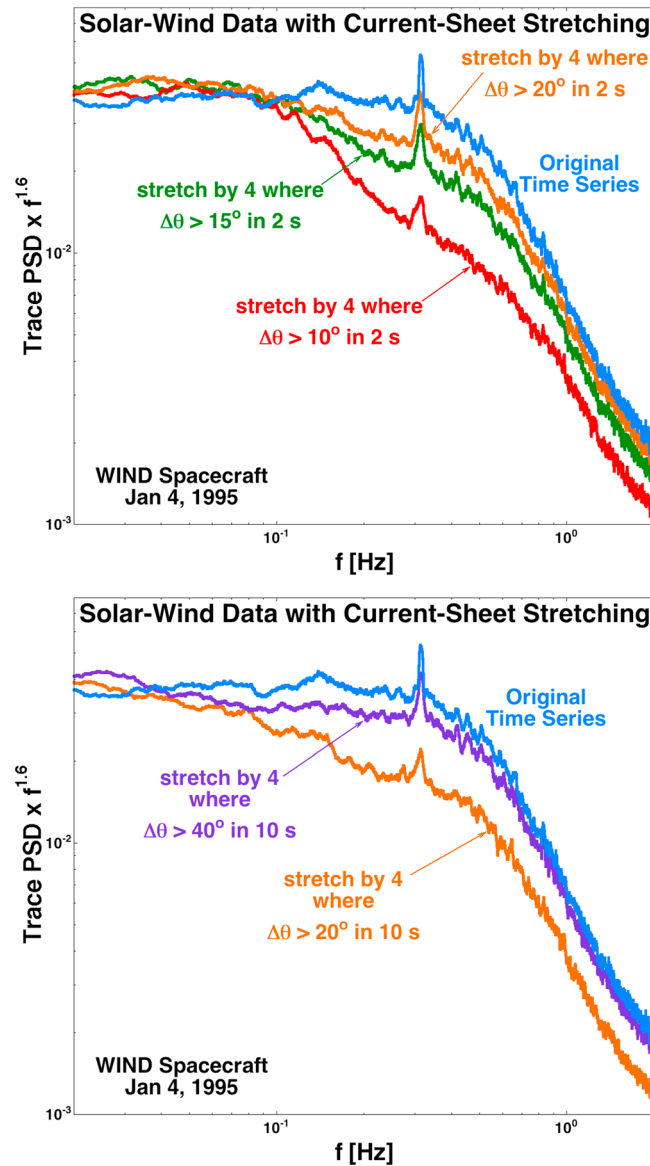
**Figure 7.** Compensated spectra for the 4 January 1995 solar wind data and for that data with current sheets stretched in time by a factor of 4. (top) The current sheets are identified in the time series by 2 s changes in the magnetic field direction and (bottom) the current sheets are identified in the time series by 10 s changes in the magnetic field direction. All plotted spectra have been smoothed with 500-point running averages.

three colors being the three GSE components of the magnetic field. The time interval in Figure 6 (top) demarked by the purple dashed vertical lines is a current sheet. In the Figure 6 (bottom) the modified time series of the solar wind magnetic field is plotted. Here the current sheet interval of Figure 6 (top) is stretched in time by a factor of 4 using the algorithm of expressions 2a, 2b, 2c, 2d, 2e applied at every data point in the current sheet interval. In the bottom panel the purple vertical dashed lines demark the current sheet interval that was time stretched. Outside of that interval the data time series is unaltered. (Note, however, that the unstretched fragments of the time series are shifted in time because of the current sheet stretching.) The effect of the stretching is to thicken the current sheet and slow down the time scales of change within the current sheet.

Figure 7 examines the power spectral densities of the Wind 4 January 1995 time series when current sheets in the time series are identified and time stretched. In Figure 7 (top) current sheets are identified when the magnetic field direction changes by more than the angular value $\Delta\theta$ in 2 s. The orange curve is for sheets with $\Delta\theta > 20°$ in 2 s, the green curve is for sheets with $\Delta\theta > 15°$ in 2 s, and the red curve is for sheets with $\Delta\theta > 10°$ in 2 s. The smaller the $\Delta\theta$ value, the larger the number of current sheets stretched (for instance, the $\Delta\theta > 10°$ set includes the $\Delta\theta > 15°$ set, which includes the $\Delta\theta > 20°$ set). Every data point in the time series when the $\Delta\theta$ criterion is triggered is time stretched, as is every

data point within $\pm 0.5$ s of a triggered point. (Hence, the interior of each current sheet is time stretched and so are the edges of the ramp.). Comparing the orange $\Delta\theta > 20°$ curve with the blue original time series curve, it is seen that the Fourier power at the breakpoint frequency is reduced by about a factor of 2 by stretching the $\Delta\theta > 20°$ current sheets in the time series. For the orange curve, 2.6% of the data points in the time series were stretched. Hence, 2.6% of the time signal contained about half of the Fourier power at the spectral breakpoint. The green ($\Delta\theta > 15°$) and red ($\Delta\theta > 10°$) curves in Figure 7 (top) show further reductions of the Fourier power at the breakpoint as weaker current sheets are time stretched in addition to the strong current sheets. Note in the orange, green, and red curves a secondary breakpoint forming at a frequency about 4 times lower than the original breakpoint owing to the stretching by a factor of 4 of time in the current sheets.
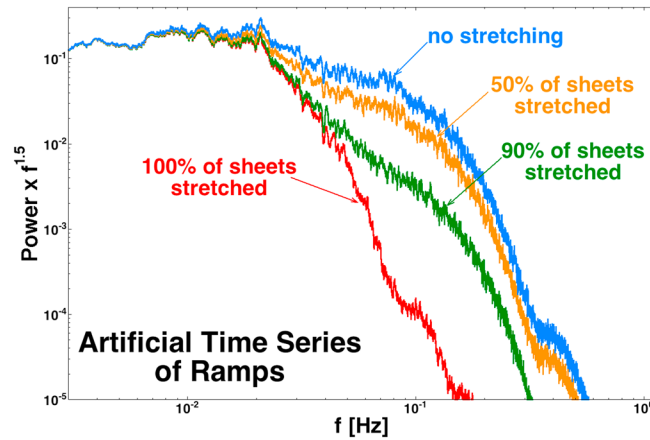
**Figure 8.** The blue curve is the power spectral density of an artificial time series with current sheets that have thicknesses between 2 and 4 s. The other colors are the power spectral densities of the artificial time series with a fraction of the current sheets stretched in time by a factor of 4: the orange curve has 50% of the current sheets stretched, the green curve has 90% of the current sheets stretched, and the red curve has 100% of the current sheets stretched.

In Figure 7 (bottom) current sheets are identified in the Wind 4 January time series by changes in the magnetic field direction occurring in a time of 10 s. The purple curve is for data with current sheets time stretched if $\Delta\theta$ is greater than 40° in 10 s. Comparing this purple curve with the original data blue curve, it is seen that stretching those current sheets produces a decrease in the Fourier power at the breakpoint by about a factor of 2. These current sheets occupy 2.2% of the data points in the time series. Hence, 2.2% of the time signal contains about half of the Fourier power at the break-point. The orange curve in Figure 7 (bottom) is for current sheets stretched if $\Delta\theta > 20°$ in 10 s, leading to a further reduction in the Fourier power at the breakpoint as weaker current sheets are stretched in the solar wind data in addition to the strong sheets.

For comparison, Figure 8 shows the power spectral density curves for several artificial time series similar to the series that were shown in Figure 2. The blue curve in Figure 8 is for an artificial time series in which all "current sheets" have widths $\Delta t$ between 2 s and 4 s (similar to the orange curve of Figure 3). In the orange curve of Figure 8 half of the current sheets (randomly chosen) in the artificial time series are stretched by a factor of 4 to have thicknesses $\Delta t$ between 8 s and 16 s. In the green curve 90% of the current sheets (randomly chosen) in the artificial time series are stretched by a factor of 4. In the red curve 100% of the current sheets in the artificial time series have been time stretched by a factor of 4. In Figure 8 the transition of the power spectral density can be seen as more and more current sheets are stretched. Note the decrease in the Fourier power at the breakpoint (at $f \sim 0.13$ Hz) as more and more current sheets are time stretched. In Figure 9 the ratios of the power spectral densities with stretching to the power spectral density without stretching are plotted. An additional curve (purple) for the case in which 10% of the current sheets are stretched is used. As can be seen, the larger the fraction of current sheets that are stretched in the time series,
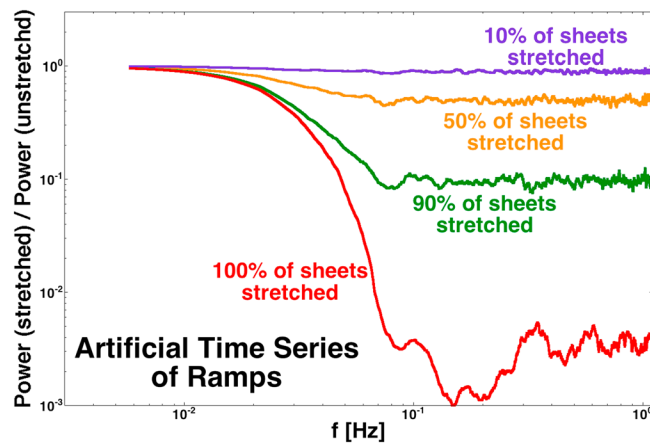


**Figure 9.** From Figure 8, the ratios are plotted of the power in various power spectral densities associated with a fraction of the current sheets being time stretched to the power spectral density of the time series without any stretching. The original current sheets had thicknesses of 2–4 s, and when a current sheet is stretched, it is stretched by a factor of 4.

the lower the ratio. For the orange curve in Figure 9, which is the ratio of the power for 50% of the current sheets stretched to the power for no current sheets stretched, at the breakpoint frequency of about 0.13 Hz the power is decreased by about a factor of 2; for the green curve in Figure 9, which is the ratio of the power for 90% of the current sheets stretched to the power for no current sheets stretched, at the breakpoint frequency of about 0.13 Hz the power is decreased by about a factor of 10. The factor-of-about-2 decreases seen in Figure 7 are indeed indicative of about half of the Fourier power being locked up in the stronger current sheets. Note also in Figure 9 the appearance of a secondary breakpoint at a frequency about a factor of 4 lower than the

original (black curve) breakpoint. These transition curves for the artificial time series in Figure 8 resemble the power spectral densities of the solar wind data in Figure 7, where the current sheets in the solar wind data are time stretched.

## 5. Summary

It is reasonable to conclude from the analysis of this study that current sheet thickness plays a role in determining the frequency $f_B$ of the high-frequency breakpoint of the magnetic power spectrum of the solar wind. Altering the temporal profile of current sheets in the time series of solar wind measurements has significant effects on the Fourier spectrum in the vicinity of the breakpoint; specifically, widening the current sheets lowers the frequency of the breakpoint. It follows that the physics that controls the current sheet thicknesses is the physics that determines the high-frequency break in the magnetic field spectrum.

Major unknowns are (1) the origins of the solar wind current sheets (cf. section 1) and (2) the plasma physical processes that control current sheet thicknesses in the solar wind (cf. Appendix A).

## Appendix A: Time Scales of Advected Ion Gyroradii and Ion Inertial Length Spatial Scales

An effective limit for the thinness of a current sheet in a collisionless plasma may be the ion kinetic scales $r_{gi} = v_{Ti}/\omega_{ci}$ (thermal ion gyroradius) [e.g., *Sasunov et al.*, 2015] and $\delta = c/\omega_{pi}$ (ion skin depth or ion inertial length) [e.g., *Singh et al.*, 2006]. Thicker current sheets may also form substructure at those ion kinetic scales [cf. *Schindler and Hesse*, 2008, 2010]. Physical processes that may limit current sheet thicknesses to the ion gyroradius or the ion inertial length could be (1) lower hybrid drift instabilities [*Daughton*, 2003; *Huang et al.*, 2009] and drift-kink instabilities [*Daughton*, 1998; *Horiuchi and Sato*, 1999], (2) modified two-stream or kinetic whistler instabilities [*Wu et al.*, 1983; *Wang et al.*, 2008], (3) Kelvin-Helmholtz-type instabilities [*Neugebauer et al.*, 1986; *Lapenta et al.*, 2003], (4) Landau damping associated with parallel electric fields [*Fejer and Kan*, 1969; *Stefant*, 1970; *Gary and Borovsky*, 2008; *Podesta et al.*, 2010], or (5) the onset of magnetic field line reconnection [*Yin and Winske*, 2002; *Scholer et al.*, 2003; *Roytershteyn and Daughton*, 2008; *Birn and Hesse*, 2014]. The very strong current sheets of the solar wind tend to be thicker than these ion kinetic scale lengths [*Siscoe et al.*, 1968; *Vasquez et al.*, 2007; *Borovsky and Steinberg*, 2014], whereas current sheets with thicknesses that are less than $r_{gi}$ or $c/\omega_{pi}$ have been seen with very high-resolution measurements in the solar wind [*Perri et al.*, 2012; *Goldstein et al.*, 2015].

For the 4 January 1995 data used in this report, $r_{gi} \sim c/\omega_{pi} \sim 115$ km (cf. section 4). With a solar wind speed of 660 km/s, a current sheet that has a thickness $w$ that is $r_{gi} \sim c/\omega_{pi} \sim 115$ km would be advected past a spacecraft in a time $\Delta t = w/v_{sw} \approx 0.17$ s if the current sheet normal was parallel to the solar wind velocity vector. This advection time scale would correspond to a Fourier spectrum breakpoint of $f_B = (\pi \Delta t)^{-1} \sim 1.8$ Hz. The current sheets in the solar wind tend to have their normals oriented perpendicular to the Parker spiral direction [*Turner and Siscoe*, 1971; *Borovsky*, 2008; *Malaspina and Gosling*, 2012; *Lukacs and Erdos*, 2013]; at 660 km/s the Parker spiral direction is 35.5° from radial. A current sheet that has a thickness $w$ will have a thickness projected in the radial direction of at least $w/\sin(35.3°) = 1.9w$. Taking $w$ to be 115 km, this would correspond to a breakpoint frequency of $f \sim 0.95$ Hz. Depending on the orientation of the current sheet normal around the Parker spiral direction, the radial thickness of the current sheet will vary from $1.9w$ a value much larger than $1.9w$, probably limited by scale size of ripples in the flatness of the current sheets or by the breadth of the current sheets, which are probably on the order of $50 R_E$ [cf. *Richardson and Paularena*, 2001; *Weimer et al.*, 2002; *Malaspina and Gosling*, 2012]. Looking at the statistics for current sheets with random orientations about the Parker spiral, the median radial thickness is a factor of 1.4 greater than the value $1.9w$. Hence, an effective median radial thickness for randomly oriented current sheets that have normal thicknesses of $w$ is in the ballpark of $2.7w$. For $w = 115$ km, this gives an effective thickness of 330 km, which passes a spacecraft in 0.4 s for a wind speed of 660 km/s. This corresponds to a breakpoint frequency $f_B = (\pi \Delta t)^{-1} \sim 0.7$ Hz. This is in the ballpark of the breakpoint frequency of about 0.4 Hz seen for the original Wind 4 January time series (blue curves in Figure 7).

Using hourly averaged solar wind measurements in the OMNI2 data set [*King and Papitashvili*, 2005] for the years 1963–2014, statistical estimates of breakpoint frequency in the solar wind for current sheets of
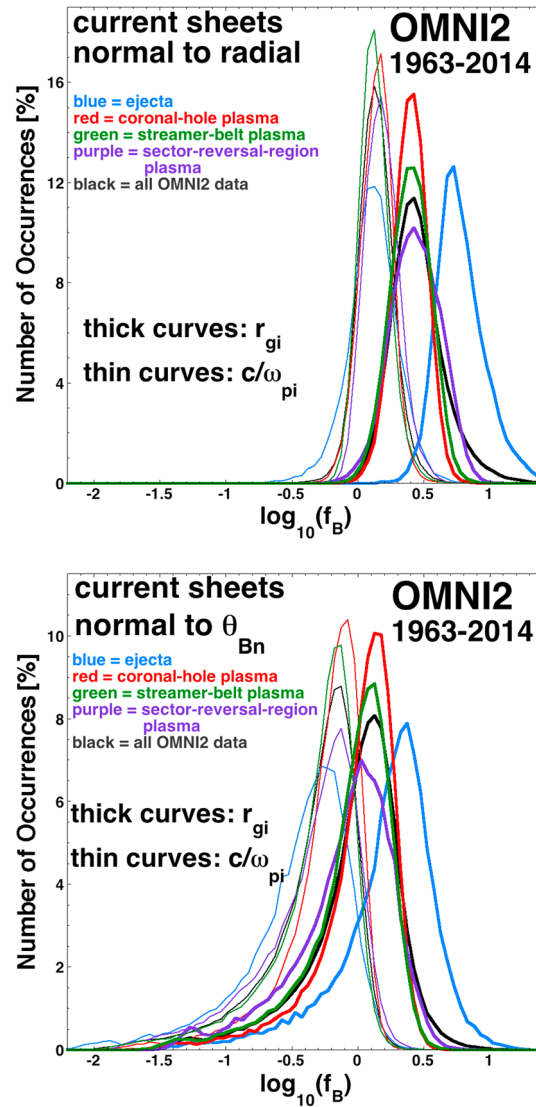
**Figure 10.** Occurrence distributions of the frequency $v_{sw}/(\pi r_{gi})$ (thick curves) and the frequency $v_{sw}/(\pi(c/\omega_{pi}))$ (thin curves) for the hourly averaged OMNI2 data set for the years 1963–2014. It is assumed that (top) the current sheets with thicknesses $r_{gi}$ or $c/\omega_{pi}$ have their normal in the radial direction and (bottom) the current sheets have their normals isotropically distributed perpendicular to the mean magnetic field, with the 1 h average field from OMNI used as the direction of that mean field.

thicknesses $r_{gi}$ and $c/\omega_{pi}$ are produced and binned in Figure 10. For current sheets with normals in the radial direction, the breakpoint frequencies $v_{sw}/(\pi r_{gi})$ and $v_{sw}/(\pi(c/\omega_{pi}))$ are calculated for every hour of data in the OMNI2 data set using the hourly averaged values of the solar wind speed $v_{sw}$, solar wind number density $n$, solar wind proton temperature $T_i$, and solar wind magnetic field strength $B_{mag}$; the base 10 logarithm of those frequencies are binned in Figure 10 (top). The thick curves are the values of $v_{sw}/(\pi r_{gi})$, and the thin curves are the values of $v_{sw}/(\pi(c/\omega_{pi}))$. The black curves are for all of the OMNI2 data. The curves in the four colors are the distributions of $v_{sw}/(\pi r_{gi})$ and $v_{sw}/(\pi(c/\omega_{pi}))$ for a categorization of the OMNI2 data into four types of solar wind plasma as described in *Xu and Borovsky* [2015]. In general, the two frequencies $v_{sw}/(\pi r_{gi})$ and $v_{sw}/(\pi(c/\omega_{pi}))$ are close to each other; however, in ejecta plasma (blue curves) the frequencies can be well separated.

In Figure 10 (bottom) the current sheets of thicknesses $r_{gi}$ and $c/\omega_{pi}$ are taken to have their normals perpendicular to the direction of the mean magnetic field and isotropically oriented around the direction of the mean magnetic field. For the direction of the mean magnetic field, the hourly averaged measured magnetic field for each hour of OMNI2 is taken. If that mean magnetic field is at an angle of $\theta_{Bn}$ to the radial direction, then the median thickness in the radial direction is $(1.4/\cos(\theta_{Bn}))r_{gi}$ for a current sheet of thickness $r_{gi}$ and $(1.4/\cos(\theta_{Bn}))c/\omega_{pi}$ for a current sheet of thickness $c/\omega_{pi}$. Hence, the median value of the breakpoint frequencies for the current sheets with normals perpendicular to the direction of the mean magnetic field will be $(\cos(\theta_{Bn})/1.4) v_{sw}/(\pi r_{gi})$ for the sheets with thicknesses $r_{gi}$ and $(\cos(\theta_{Bn})/1.4)v_{sw}/(\pi(c/\omega_{pi}))$ for the sheets with thicknesses $c/\omega_{pi}$. The base 10 logarithm of the two frequencies $(\cos(\theta_{Bn})/1.4)v_{sw}/(\pi r_{gi})$ and $(\cos(\theta_{Bn})/1.4)v_{sw}/(\pi(c/\omega_{pi}))$ are binned in Figure 10

(bottom) for the OMNI2 data set. Again, the two frequencies $(\cos(\theta_{Bn})/1.4)v_{sw}/(\pi r_{gi})$ and $(\cos(\theta_{Bn})/1.4)v_{sw}/(\pi(c/\omega_{pi}))$ are, in general, close to each other; however, in ejecta plasma (blue curves) the frequencies can be well separated. Note, however, that ejecta is characterized by a scarcity of current sheets.

## References

Barkhatov, N. A., A. V. Korolev, G. N. Zastenker, M. O. Ryazantseva, and P. A. Dalin (2003), MHD simulations of the dynamics of sharp disturbances of the interplanetary medium and comparison with spacecraft observations, *Cosmic Res.*, *41*, 529–538.

Behannon, K. W. (1978), Heliocentric distance dependence of the interplanetary magnetic field, *Rev. Geophys.*, *16*, 125–145, doi:10.1029/RG016i001p00125.

Belcher, J. W., and L. Davis (1971), Large-amplitude Alfven waves in the interplanetary medium, 2, *J. Geophys. Res.*, *76*, 3534–3563, doi:10.1029/JA076i016p03534.

Birn, J., and M. Hesse (2014), Forced reconnection in the near magnetotail: Onset and energy conversion in PIC and MHD simulations, *J. Geophys. Res. Space Physics*, *119*, 290–309, doi:10.1002/2013JA019354.

Borovsky, J. E. (2008), The flux-tube texture of the solar wind: Strands of the magnetic carpet at 1 AU?, *J. Geophys. Res.*, *113*, A08110, doi:10.1029/2007JA012684.

Borovsky, J. E. (2010), On the contribution of strong discontinuities to the power spectrum of the solar wind, *Phys. Rev. Lett.*, *105*, 111102.

Borovsky, J. E. (2012a), Looking for evidence of mixing in the solar wind from 0.31 to 0.98 AU, *J. Geophys. Res.*, *117*, A06107, doi:10.1029/2012JA017525.

Borovsky, J. E. (2012b), The effect of sudden wind shear on the Earth's magnetosphere: Statistics of wind-shear events and CCMC simulations of magnetotail disconnections, *J. Geophys. Res.*, *117*, A06224, doi:10.1029/2012JA017623.

Borovsky, J. E. (2012c), The velocity and magnetic-field fluctuations of the solar wind at 1 AU: Statistical analysis of Fourier spectra and correlations with plasma properties, *J. Geophys. Res.*, *117*, A05104, doi:10.1029/2011JA017499.

Borovsky, J. E., and J. T. Steinberg (2014), No evidence for the localized heating of solar-wind protons at intense velocity shear zones, *J. Geophys. Res. Space Physics*, *119*, 1455, doi:10.1002/2013JA019746.

Bourouaine, S., O. Alexandrova, E. Marsch, and M. Maksimovic (2012), On spectral breaks in the power spectra of magnetic fluctuations in fast solar wind between 0.3 and 0.9 AU, *Astrophys. J.*, *749*, 102.

Bruno, R., and L. Trenchi (2014), Radial dependence of the frequency break between fluid and kinetic scales in the solar wind fluctuations, *Astrophys. J. Lett.*, *787*, L24.

Bruno, R., and V. Carbone (2013), The solar wind as a turbulence laboratory, *Living Rev. Solar Phys. 10*, 2. [Available at http://www.livingreview.org/lrsp-2013-2.]

Bruno, R., V. Carbone, P. Veltri, E. Pietropaolo, and B. Bavassano (2001), Identifying intermittency events in the solar wind, *Planet. Space Sci.*, *49*, 1201–1210.

Burlaga, L. F. (1969), Directional discontinuities in the interplanetary magnetic field, *Solar Phys.*, *7*, 54–71.

Burlaga, L. F., and N. F. Ness (1969), Tangential discontinuities in the solar wind, *Solar Phys.*, *9*, 467.

Cardona, M., R. V. Chamberlin, and W. Marx (2007), The history of the stretched exponential function, *Ann. Phys.*, *16*, 842.

Chen, C. H. K., L. Leung, S. Boldyrev, B. A. Maruca, and S. D. Bale (2014), Ion-scale spectral break of solar wind turbulence at high and low beta, *Geophys. Res. Lett.*, *41*, 8081–8088, doi:10.1002/2014GL062009.

Dalin, P. A., G. N. Zastenker, K. I. Paularena, and J. D. Richardson (2002), A survey of large, rapid solar wind dynamic pressure changes observed by Interball-1 and IMP 8, *Ann. Geophys.*, *20*, 293–299.

Daughton, W. (1998), Kinetic theory of the drift kink instability in a current sheet, *J. Geophys. Res.*, *103*, 29,429–29,443, doi:10.1029/1998JA900028.

Daughton, W. (2003), Electromagnetic properties of the lower-hybrid drift instability in a thin current sheet, *Phys. Plasmas*, *10*, 3103.

Dishon, M., G. H. Weill, and J. T. Bender (1985), Stable law densities and linear relaxation phenomena, *J. Res. Nat. Bureau Stand.*, *90*, 27.

Fejer, J. A., and J. R. Kan (1969), A guiding centre Vlasov equation and its application to Alfven waves, *J. Plasma Phys.*, *3*, 331–351.

Flomenbom, O., et al. (2005), Stretched exponential decay and correlations in the catalytic activity of fluctuating single lipase molecules, *Proc. Natl. Acad. Sci. U.S.A.*, *102*, 2368–2372.

Franz, M., D. Burgess, and T. S. Horbury (2000), Magnetic field depressions in the solar wind, *J. Geophys. Res.*, *105*, 12,725–12,732, doi:10.1029/2000JA900026.

Gary, S. P. (1999), Collisionless dissipation wavenumber: Linear theory, *J. Geophys. Res.*, *104*, 6759–6762, doi:10.1029/1998JA900161.

Gary, S. P., and J. E. Borovsky (2004), Alfven-cyclotron fluctuations: Linear Vlasov theory, *J. Geophys. Res.*, *109*, A06105, doi:10.1029/2004JA010399.

Gary, S. P., and J. E. Borovsky (2008), Damping of long-wavelength kinetic Alfven fluctuations: Linear theory, *J. Geophys. Res.*, *113*, A12104, doi:10.1029/2008JA013565.

Goldstein, M. L., and D. A. Roberts (1999), Magnetohydrodynamic turbulence in the solar wind, *Phys. Plasmas*, *6*, 4154.

Goldstein, M. L., D. A. Roberts, and W. H. Matthaeus (1995), Magnetohydrodynamic turbulence in the solar wind, *Ann. Rev. Astron. Astrophys.*, *33*, 283.

Goldstein, M. L., et al. (2015), Multipoint observations of plasma phenomena made in space by Cluster, *J. Plasma Phys.*, *81*, 325810301.

Greco, A., W. H. Matthaeus, S. Servidio, P. Chuychai, and P. Dmitruk (2009), Statistical analysis of discontinuities in solar wind ACE data and comparison with intermittent MHD turbulence, *Astrophys. J.*, *691*, L111.

Horiuchi, R., and T. Sato (1999), Three-dimensional particle simulation of plasma instabilities and collisionless reconnection in a current sheet, *Phys. Plasmas*, *6*, 4565.

Howes, G. G., S. C. Cowley, W. Dorland, G. W. Hammett, E. Quataert, and A. A. Schekochihin (2008), A model of turbulence in magnetized plasmas: Implications for the dissipation range in the solar wind, *J. Geophys. Res.*, *113*, A05103, doi:10.1029/2007JA012665.

Huang, F. Y., G. Chen, Z. Shi, H. Hu, J. Z. Peng, and M. Y. Yu (2009), Lower-hybrid drift instability in a thin current sheet with κ velocity distribution, *Phys. Plasmas*, *16*, 042107.

International Telephone and Telegraph Corporation (1979), *Reference Data for Radio Engineers*, sect. 44-5, Howard Sams, Indianapolis.

King, J. H., and N. E. Papitashvili (2005), Solar wind spatial scales in and comparisons of hourly Wind and ACE plasma and magnetic field data, *J. Geophys. Res.*, *110*, A02104, doi:10.1029/2004JA010649.

Laherrere, J., and D. Sornette (1998), Stretched exponential distributions in nature and economy: "Fat tails" with characteristic scales, *Eur. Phys. J. B*, *2*, 525–539.

Lapenta, G., J. U. Brackbill, and W. S. Daughton (2003), The unexpected role of the lower hybrid drift instability in magnetic reconnection in three dimensions, *Phys. Plasmas*, *10*, 1577.

Leamon, R. J., C. W. Smith, N. F. Ness, W. H. Matthaeus, and H. K. Wong (1998), Observational constraints on the dynamics of the interplanetary magnetic field dissipation range, *J. Geophys. Res.*, *103*, 4775–4787, doi:10.1029/97JA03394.

Leamon, R. J., C. W. Smith, N. F. Ness, and H. K. Wong (1999), Dissipation range dynamics: Kinetic Alfven waves and the importance of $\beta_e$, *J. Geophys. Res.*, *104*, 22,331–22,344, doi:10.1029/1999JA900158.

Leamon, R. J., W. H. Matthaeus, C. W. Smith, G. P. Zank, D. J. Mullan, and S. Oughton (2000), MHD-driven kinetic dissipation in the solar wind and corona, *Astrophys. J.*, *537*, 1054.

Lepping, R. P., et al. (1995), The WIND magnetic field investigation, *Space Sci. Rev.*, *71*, 207.

Li, G. (2008), Identifying currentsheet-like structures in the solar wind, *Astrophys. J.*, *672*, L65–L68.

Li, G., B. Miao, Q. Hu, and G. Qin (2011), Effect of current sheets on the solar wind magnetic field power spectrum from the Ulysses observation: From Kraichnan to Kolmogorov scaling, *Phys. Rev. Lett.*, *106*, 125001.

Lukacs, K., and G. Erdos (2013), Angular distribution of discontinuity normal of the interplanetary magnetic field, *Astron. Nachr.*, *334*, 1055–1058.

Malaspina, D. M., and J. T. Gosling (2012), Two spacecraft observations of magnetic discontinuities in the solar wind with STEREO, *J. Geophys. Res.*, *117*, A04109, doi:10.1029/2011JA017375.

Mangeney, A., C. Salem, P. L. Veltri, and B. Cecconi (2001), Intermittency in the solar wind turbulence and the Haar wavelet transform, *ESA Spec. Publ. ESA*, *SP-492*, 53.

Markovskii, S. A., B. J. Vasquez, and C. W. Smith (2008), Statistical analysis of the high-frequency spectral break of the solar wind turbulence at 1 AU, *Astrophys. J.*, *675*, 1576.

Montroll, E. W., and J. T. Bender (1984), On Levy (or stable) distribution and the Williams-Watts model of dielectric relaxation, *J. Stat. Phys.*, *34*, 129–162.

Neugebauer, M. (1985), Alignment of velocity and field changes across tangential discontinuities in the solar wind, *J. Geophys. Res.*, *90*, 6627–6630, doi:10.1029/JA090iA07p06627.

Neugebauer, M. (2006), Comment on the abundances of rotational and tangential discontinuities in the solar wind, *J. Geophys. Res.*, *111*, A04103, doi:10.1029/2005JA011497.

Neugebauer, M., and C. J. Alexander (1991), Shuffling foot points and magnetohydrodynamic discontinuities in the solar wind, *J. Geophys. Res.*, *96*, 9409–9418, doi:10.1029/91JA00566.

Neugebauer, M., and J. Giacalone (2010), Progress in the study of interplanetary discontinuities, *AIP Conf. Proc.*, *1216*, 194.

Neugebauer, M., D. R. Clay, B. E. Goldstein, B. T. Tsurutani, and R. D. Zwickl (1984), A reexamination of rotational and tangential discontinuities in the solar wind, *J. Geophys. Res.*, *89*, 5395–5408, doi:10.1029/JA089iA07p05395.

Neugebauer, M., C. J. Alexander, R. Schwenn, and A. K. Richter (1986), Tangential discontinuities in the solar wind: Correlated field and velocity changes and the Kelvin-Helmholtz instability, *J. Geophys. Res.*, *91*, 13,694–13,698, doi:10.1029/JA091iA12p13694.

Otnes, R. K., and L. Enochson (1972), *Digital Time Series Analysis*, chap. 5 and 6, Wiley, New York.

Owens, M. J., R. T. Wicks, and T. S. Horbury (2011), Magnetic discontinuities in the near-Earth solar wind: Evidence of in-transit turbulence or remnants of coronal structure?, *Solar Phys.*, *269*, 411–420.

Pennetta, C. (2006), Distribution of return intervals in extreme events, *Eur. Phys. J. B*, *50*, 95.

Percival, D. B., and A. T. Walden (1993), *Spectral Analysis for Physical Applications*, Cambridge Univ. Press, Cambridge.

Perri, S., M. L. Goldstein, J. C. Dorelli, and F. Sahraoui (2012), Detection of small-scale structures in the dissipation regime of solar-wind turbulence, *Phys. Rev. Lett.*, *109*, 191101.

Podesta, J. J. (2012), The need to consider ion Bernstein waves as a dissipation channel of solar wind turbulence, *J. Geophys. Res.*, *117*, A07101, doi:10.1029/2012JA017770.

Podesta, J. J., D. A. Roberts, and M. L. Goldstein (2007), Spectral exponents of kinetic and magnetic energy spectra in solar wind turbulence, *Astrophys. J.*, *664*, 543.

Podesta, J. J., J. E. Borovsky, and S. P. Gary (2010), A kinetic Alfven wave cascade subject to collisionless damping cannot reach electron scales in the solar wind at 1 AU, *Astrophys. J.*, *712*, 685.

Riazantseva, M. O., G. N. Zastenker, and J. D. Richardson (2005a), The characteristics of sharp (small-scale) boundaries of solar wind plasma and magnetic field structures, *Adv. Space Res.*, *35*, 2147.

Riazantseva, M. O., G. N. Zastenker, J. D. Richardson, and P. E. Eiges (2005b), Sharp boundaries of small- and middle-scale solar wind structures, *J. Geophys. Res.*, *110*, A12110, doi:10.1029/2005JA011307.

Richardson, J. D., and K. I. Paularena (2001), Plasma and magnetic field correlations in the solar wind, *J. Geophys. Res.*, *106*, 239–251, doi:10.1029/2000JA000071.

Roberts, D. A. (2012), Construction of solar-wind-like magnetic fields, *Phys. Rev. Lett.*, *109*, 231102.

Roytershteyn, V., and W. Daughton (2008), Collisionless instability of thin current sheets in the presence of sheared parallel flows, *Phys. Plasmas*, *15*, 082901.

Sahraoui, F., M. L. Goldstein, G. Belmont, P. Canu, and L. Rezeau (2010), Three dimensional anisotropic k spectra of turbulence at subproton scales in the solar wind, *Phys. Rev. Lett.*, *105*, 131101.

Sahraoui, F., G. Belmont, and M. L. Goldstein (2012), New insight into short-wavelength solar wind fluctuations from Vlasov theory, *Astrophys. J.*, *748*, 100.

Saito, S., S. P. Gary, and Y. Narita (2010), Wavenumber spectrum of whistler turbulence: Particle-in-cell simulation, *Phys. Plasmas*, *17*, 122316.

Sari, J. W., and N. F. Ness (1969), Power spectra of the interplanetary magnetic field, *Solar Phys.*, *8*, 155.

Sasunov, Y. L., M. L. Khodachenko, I. I. Alexeev, E. S. Belenkaya, V. S. Semenov, I. V. Kubyshkin, and O. V. Mingalev (2015), Investigation of scaling properties of a thin current sheet by means of particle trajectories study, *J. Geophys. Res. Space Physics*, *120*, 1633–1645, doi:10.1002/2014JA020486.

Schindler, K., and M. Hesse (2008), Formation of thin bifurcated current sheets by quasisteady compression, *Phys. Plasmas*, *15*, 042902.

Schindler, K., and M. Hesse (2010), Conditions for the formation of nongyrotropic current sheets in slowly evolving plasmas, *Phys. Plasmas*, *17*, 082103.

Scholer, M., I. Sidorenko, C. H. Jaroschek, R. A. Treumann, and A. Zeiler (2003), Onset of collisionless magnetic reconnection in thin current sheets: Three-dimensional particle simulations, *Phys. Plasmas*, *10*, 351.

Simdyankin, S. I., and N. Mousseau (2003), Relationship between dynamical heterogeneities and stretched exponential relaxation, *Phys. Rev. E*, *68*, 041110.

Singh, N., C. Deverapalli, and G. Khazanov (2006), Electrodynamics in a very thin current sheet leading to magnetic reconnection, *Nonlinear. Process. Geophys.*, *13*, 509.

Siscoe, G. L., L. Davis, P. J. Coleman, E. J. Smith, and D. E. Jones (1968), Power spectra and discontinuities of the interplanetary magnetic field: Mariner 4, *J. Geophys. Res.*, *73*, 61–82, doi:10.1029/JA073i001p00061.

Stawicki, O., S. P. Gary, and H. Li (2001), Solar wind magnetic fluctuation spectra: Dispersion and damping, *J. Geophys. Res.*, *106*, 8273–8281, doi:10.1029/2000JA000446.

Stefant, R. J. (1970), Alfven wave damping from finite gyroradius coupling to the ion acoustic mode, *Phys. Fluids*, *13*, 440.

TenBarge, J. M., J. J. Podesta, K. G. Klein, and G. G. Howes (2012), Interpreting magnetic variance anisotropy measurements in the solar wind, *Astrophys. J.*, *735*, 107.

Tennekes, H., and J. L. Lumley (1972), *A First Course in Turbulence*, MIT Press, Cambridge.

Thomson, D. J. (1982), Spectrum estimation and harmonic analysis, *Proc. IEEE*, *70*, 1055.

Tsurutani, B. T., and C. M. Ho (1999), A review of discontinuities and Alfven waves in interplanetary space: ULYSSES results, *Rev. Geophys.*, *37*, 517–541, doi:10.1029/1999RG900010.

Tu, C.-Y., and E. Marsch (1995), MHD structures, waves and turbulence in the solar wind, *Space Sci. Rev.*, *73*, 1.

Turner, J. M., and G. L. Siscoe (1971), Orientations of 'rotational' and 'tangential' discontinuities in the solar wind, *J. Geophys. Res.*, *76*, 1816, doi:10.1029/JA076i007p01816.

Vasquez, B. J., and J. V. Hollweg (1999), Formation of pressure-balanced structures and fast waves from nonlinear Alfven waves, *J. Geophys. Res.*, *104*, 4681, doi:10.1029/1998JA900090.

Vasquez, B. J., V. I. Abramenko, D. K. Haggerty, and C. W. Smith (2007), Numerous small magnetic field discontinuities of Bartels rotation 2286 and the potential role of Alfvenic turbulence, *J. Geophys. Res.*, *112*, A11102, doi:10.1029/2007JA012504.

Veltri, P. (1999), MHD turbulence in the solar wind: Self-similarity, intermittency and coherent structures, *Plasma Phys. Control. Fusion*, *41*, A787.

Wang, X. Y., Y. Lin, L. Chen, and Z. Lin (2008), Particle simulation of current sheet instabilities under finite guide field, *Phys. Plasmas*, *15*, 072103.

Weimer, D. R., D. M. Ober, N. C. Maynard, W. J. Burke, M. R. Collier, D. J. McComas, N. F. Ness, and C. W. Smith (2002), Variable time delays in the propagation of the interplanetary magnetic field, *J. Geophys. Res.*, *107*, 1210, doi:10.1029/2001JA009102.

Wu, C. S., Y. M. Zhau, S. T. Tsai, S. C. Guo, D. Winske, and K. Papadopoulos (1983), A kinetic cross-field streaming instability, *Phys. Fluids*, *26*, 1259.

Wuttke, J. (2012), Laplace-Fourier transform of the stretched exponential function: Analytic error bounds, double exponential transform, and open-source implementation "libkww", *Algorithms*, *5*, 604.

Xu, F., and J. E. Borovsky (2015), A new 4-plasma categorization scheme for the solar wind, *J. Geophys. Res. Space Physics*, *120*, 70–100, doi:10.1002/2014JA020412.

Yin, L., and D. Winske (2002), Simulation of current sheet thinning and reconnection, *J. Geophys. Res.*, *107*(A12), 1485, doi:10.1029/2002JA009507.

Zhdankin, V., S. Boldyrev, J. Mason, and J. C. Perez (2012), Magnetic discontinuities in magnetohydrodynamic turbulence and in the solar wind, *Phys. Rev. Lett.*, *108*, 175004.